JACS Au
AN OPEN ACCESS JOURNAL OF THE AMERICAN CHEMICAL SOCIETY

pubs.acs.org/jacsau

Article

Surface Reconstruction and Passivation of $BiVO_4$ Photoanodes Depending on the "Structure Breaker" Cs^+

Chen Tao, Yi Jiang,* Yunxuan Ding, Bingquan Jia, Ruitong Liu, Peifeng Li, Wenxing Yang, Lixin Xia, Licheng Sun, and Biaobiao Zhang*

Cite This: *JACS Au* 2023, 3, 1851−1863

Read Online

ACCESS | Metrics & More | Article Recommendations | Supporting Information

ABSTRACT: Monoclinic $BiVO_4$ is one of the most promising photoanode materials for solar water splitting. The photoelectrochemical performance of a $BiVO_4$ photoanode could be significantly influenced by the noncovalent interactions of redox-inert metal cations at the photoanode−electrolyte interfaces, but this point has not been well investigated. In this work, we studied the Cs^+-dependent surface reconstruction and passivation of $BiVO_4$ photoanodes. Owing to the "structure breaker" nature of Cs^+, the Cs^+ at the $BiVO_4$ photoanode−electrolyte interfaces participated in $BiVO_4$ surface photocorrosion to form a Cs^+-doped bismuth vanadium oxide amorphous thin layer, which inhibited the continuous photocorrosion of $BiVO_4$ and promoted surface charge transfer and water oxidation. The resulting cocatalyst-free $BiVO_4$ photoanodes achieved 3.3 mA cm^{-2} photocurrent for water oxidation. With the modification of FeOOH catalysts, the photocurrent at 1.23 V_{RHE} reached 5.1 mA cm^{-2}, and a steady photocurrent of 3.0 mA cm^{-2} at 0.8 V_{RHE} was maintained for 30 h. This work provides new insights into the understanding of Cs^+ chemistry and the effects of redox-inert cations at the electrode−electrolyte interfaces.

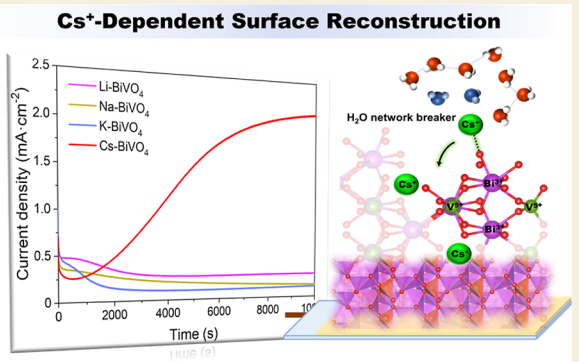

KEYWORDS: *water oxidation, $BiVO_4$, cesium, cation effect, water splitting*

INTRODUCTION

Photoelectrochemical (PEC) water splitting by semiconductor photoanodes offers a promising way to convert solar energy to hydrogen energy. Monoclinic bismuth vanadate ($BiVO_4$) is an attractive and widely researched photoanode material owing to its appropriate band gap of 2.4 eV, light absorption up to 540 nm, matching band edge for water splitting, long carrier lifetime of 40 ns, nontoxicity, and low cost. However, the PEC water splitting performance of the pristine $BiVO_4$ photoanode is largely hampered by its short electron-diffusion length and sluggish water oxidation kinetics.[1] Based on various validated strategies such as morphology engineering,[2] heterostructure formation,[3−5] element doping,[6,7] crystal facet engineering,[8,9] and modification of water-oxidation catalysts,[10−13] the benchmark water-splitting photocurrent by $BiVO_4$ photoanodes has exceeded 5.0 mA cm^{-2}, approaching its estimated maximum of 7.5 mA cm^{-2}.

Alkali and alkaline metal cations are of great importance in chemical and biological redox processes.[14−16] For instance, Ca^{2+} plays a pivotal role in water oxidation through the Mn_4CaO_5 oxygen-evolving complex (OEC),[17] and Zn^{2+} greatly affects the dismutation of $O_2^{\bullet-}$ in copper-zinc superoxide dismutase (CuZn-SOD).[18] It has also been reported that noncovalent interactions of redox-inert metal cations with metal−oxygen species can regulate the reactivity of high-valent metal-oxo, peroxo, and superoxo species.[19,20] Since the PEC water oxidation takes place at the $BiVO_4$ photoanode−electrolyte interfaces, cations in the electrolyte may interact with the surface high-valent bismuth−oxygen and vanadium−oxygen species.[21] Therefore, the PEC performance is indeed dependent on both the electrode and the electrolyte; however, there has been less research on the latter.

Cs^+ has the largest ionic radius among the nonradiative cations.[22] Consequently, it has the lowest Lewis acidity and electronegativity and the highest molar conductivity; its corresponding alkali hydroxide has the highest basicity.[22] The Cs^+ in aqueous solution is a "structure breaker," which generates less structured H_2O network, more isolated H_2O, and partially desolvated Cs^+.[23,24] In studies of the cation effect on Pt electro-catalyzed oxygen reduction, hydrogen oxidation, and methanol oxidation, the best catalytic performance was obtained when electrolytes contain Cs^+ because Cs^+ and the adsorbed hydroxyl on Pt have the weakest noncovalent

Received: February 27, 2023
Revised: May 16, 2023
Accepted: May 16, 2023
Published: July 13, 2023

https://doi.org/10.1021/jacsau.3c00100
JACS Au 2023, 3, 1851−1863

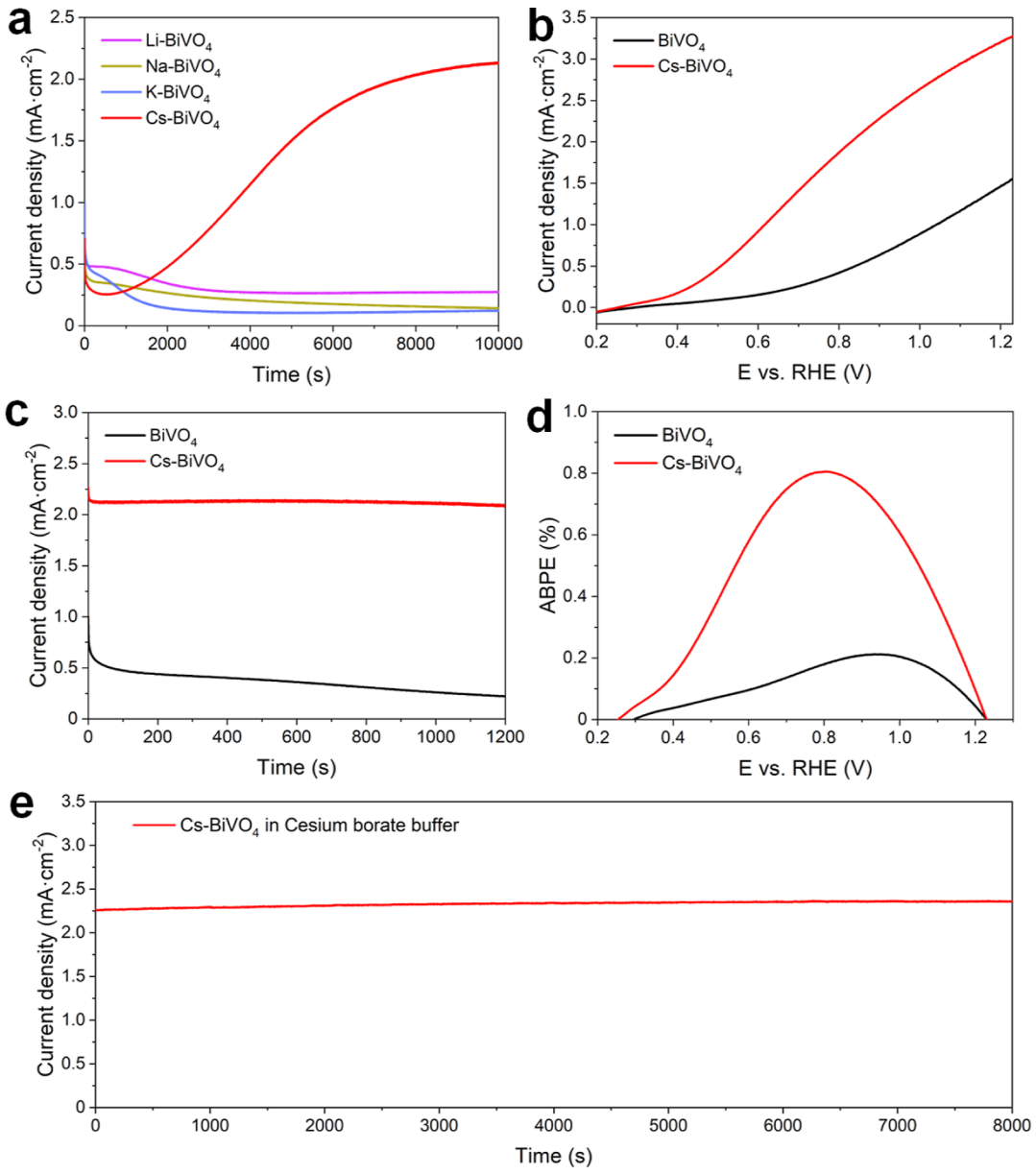

Figure 1. (a) $J-t$ curves of $BiVO_4$ at 0.8 V_{RHE} bias in different borate buffer electrolytes. (b) $J-V$ curves of $BiVO_4$ and Cs-$BiVO_4$ photoanodes. (c) $J-t$ curves of $BiVO_4$ and Cs-$BiVO_4$ photoanodes measured at 0.8 V_{RHE}. (d) ABPEs of $BiVO_4$ and Cs-$BiVO_4$ photoanodes. (e) $J-t$ curves of Cs-$BiVO_4$ photoanodes measured at 0.8 V_{RHE}. Measurements of (b–d) were performed in 1.0 M potassium borate buffer (pH 9.5) under AM 1.5 G simulated sunlight (100 mW cm^{-2}) at a scan rate of 10 mV s^{-1}. Measurement of (e) was performed in 1.0 M cesium borate buffer (pH 9.5).

interactions.[25] In CO_2 electroreduction studies, Cs^+ stabilizes the CO_2^- intermediates and dramatically enhances the CO production efficiency.[26,27] Cs^+ shows the most significant effect on the activity and selectivity of C_{2+}-products among alkali metal ions.[28,29] In the water oxidation catalyzed by a CuF_2 complex, the catalytic performance is completely dependent on the presence of Cs^+ in the electrolyte.[28,30] More reports demonstrated that Cs^+ is essential in promoting the catalytic properties of NiOOH,[31] NiFeOOH,[32,33] and MnO_x in water oxidation.[34−36]

Owing to the intrinsic element nature of Cs^+, the Cs^+ in the electrolyte displayed unique and unexpected effects on electrocatalysis.[21,37−39] However, improving the PEC water splitting of photoanode by effects of Cs^+ at the photoanode–electrolyte interfaces has not been discovered. Herein, we first report a Cs^+-dependent surface reconstruction and passivation of $BiVO_4$ photoanodes, which is observed as a significant PEC-activation effect. The $BiVO_4$ photoanodes after Cs^+-induced PEC-activation attained a photocurrent of 3.3 mA cm^{-2} at 1.23 V_{RHE} and the onset potential of water oxidation cathodically shifted to 0.35 V_{RHE}. Control experiments, physical characterization studies, carrier dynamics studies, dark electrochemical analyses, and density functional theory (DFT) calculations were carried out to investigate the Cs^+-dependent PEC activation. As a result, the remarkable improvement in PEC water oxidation was attributed to the formation of a functional Cs^+-doped bismuth vanadium oxide amorphous thin layer (denoted as the CsBiVO layer) on the $BiVO_4$ surface via a surface reconstruction process that relies on the presence of Cs^+ in the electrolyte.

https://doi.org/10.1021/jacsau.3c00100
JACS Au 2023, 3, 1851−1863

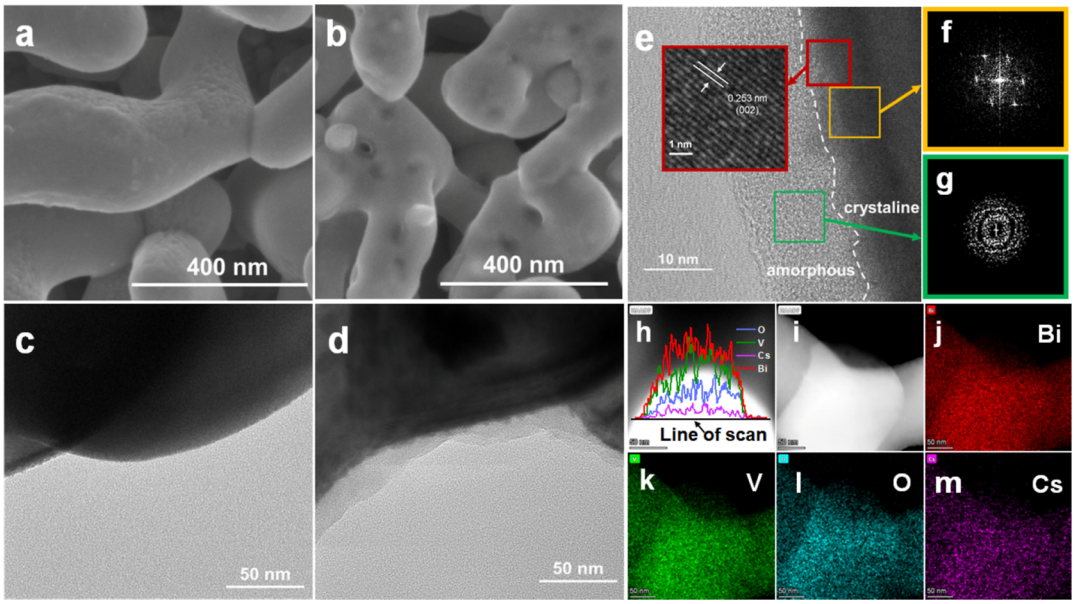

Figure 2. SEM images of (a) $BiVO_4$ and (b) Cs-$BiVO_4$. TEM images of (c) $BiVO_4$ and (d) Cs-$BiVO_4$. (e) Enlarged TEM image and FFT pattern of (f) the orange rectangle region and (g) the green rectangle region in (e). (h) TEM–EDS line analysis and (i) HAADF images of Cs-$BiVO_4$. (j–m) The corresponding EDS mapping images of (i).

RESULTS

Cs-$BiVO_4$ Formed from the Cs^+-Dependent PEC-Activation

The wormlike nanoporous $BiVO_4$ photoanodes employed in this study were prepared according to the literature and were characterized by scanning electron microscopy (SEM), X-ray diffraction (XRD), and UV–vis absorption spectroscopy (Figure S1).[40] Cs^+-dependent PEC activation was first observed in the photocurrent–time (J–t) curves of $BiVO_4$ photoanodes tested in the borate buffer solution (pH 9.5). As shown in Figure 1a, under a bias of 0.8 V_{RHE}, the photocurrent of $BiVO_4$ photoanodes in the borate buffer solutions with Li^+, Na^+, and K^+ remained stable for approximately 1000 s and then decreased gradually. This is a typical photocorrosion phenomenon of $BiVO_4$ photoanodes owing to the intrinsic stability of the $BiVO_4$ structure.[41] Surprisingly, in the borate buffer solution containing Cs^+, after a rapid decrease in the first several hundred seconds, the photocurrent began to rise continuously until it reached a plateau after 8000 s. The final stable photocurrent was approximately 10 times higher than the final photocurrent of $BiVO_4$ photoanodes tested in the borate buffer solutions with other cations. After the J–t tests, all the $BiVO_4$ photoanodes were removed from the electrolyte, rinsed with Milli-Q water, and dried under N_2 flow. The photoanodes placed in the solutions with Li^+, Na^+, K^+, and Cs^+ were denoted as Li-$BiVO_4$, Na-$BiVO_4$, K-$BiVO_4$, and Cs-$BiVO_4$, respectively. The photoanode after directly dipping in the cesium borate buffer solution for 3 h in the dark was denoted as immersion-$BiVO_4$.

The Cs^+-dependent PEC activation was then confirmed by the photocurrent–potential (J–V) curves of Li-$BiVO_4$, Na-$BiVO_4$, K-$BiVO_4$, and Cs-$BiVO_4$ in potassium borate buffer (Figure S2a) and cesium borate buffer solutions (Figure S2b). The J–V curve of Cs-$BiVO_4$ is several times higher than those of pristine $BiVO_4$, Li-$BiVO_4$, Na-$BiVO_4$, and K-$BiVO_4$. Compared to pristine $BiVO_4$ (Figure 1b), the PEC water oxidation onset potential (at J = 0.1 mA cm^{-2}) shifted from 0.53 to 0.35 V_{RHE}. A photocurrent of 3.3 mA cm^{-2} is achieved at 1.23 V_{RHE}, which is among the best performances of co-catalyst-free $BiVO_4$ photoanodes (Table S1). Under a bias of 0.8 V_{RHE}, the stable photocurrent density of Cs-$BiVO_4$ is about 10 times higher than that of pristine $BiVO_4$ (Figure 1c). The significantly enhanced PEC performance of Cs-$BiVO_4$ can also be demonstrated in the applied bias photon-to-current efficiency (ABPE, Figure 1d) and incident photon-to-current conversion efficiency (IPCE, Figure S3). The Faraday efficiency of oxygen evolution of Cs-$BiVO_4$ is 95% under 0.8 V_{RHE} (Figure S4). Regarding the stability of Cs-$BiVO_4$, a steady photocurrent density of 2.25 mA cm^{-2} lasting over 2 h is achieved when cesium borate buffer is used as an electrolyte (Figure 1e).

To reveal whether the Cs^+-dependent PEC activation also occurs for $BiVO_4$ photoanodes prepared by other methods, we made a $BiVO_4$ photoanode by using a successive ionic layer adsorption and reaction (SILAR) method.[42] The SILAR-$BiVO_4$ was then subjected to J–t test in both potassium borate buffer and cesium borate buffer solutions. As shown in Figure S5, the SILAR-$BiVO_4$ photoanode showed typical photocorrosion phenomenon for the test with potassium borate buffer, and the PEC-activation was also observed for the test with cesium borate buffer, indicating the universality of the Cs^+-dependent PEC activation. Since the cation species in the electrolytes are the only variable, the observed PEC-activation effect purely depends on Cs^+. As shown in the control experiments, illumination and bias are also necessary conditions for PEC activation (Figures S6–S8); however, the presence of Cs^+ in the electrolyte is essential. It is speculated that the Cs^+-dependent PEC activation occurs through a new underlying mechanism different from the reported photocharging[43] and borate-treatment effects.[44]

Moreover, it should be noted that Gao et al. reported the significant improvement of $BiVO_4$ photoanodes by potentiostatic photopolarization in which the electrolyte is a potassium borate buffer solution.[45] Although the cation effect was not considered in their study, the presented phenomenon is contrary to our results shown in Figure 1a. The contrast might

https://doi.org/10.1021/jacsau.3c00100
JACS Au 2023, 3, 1851–1863

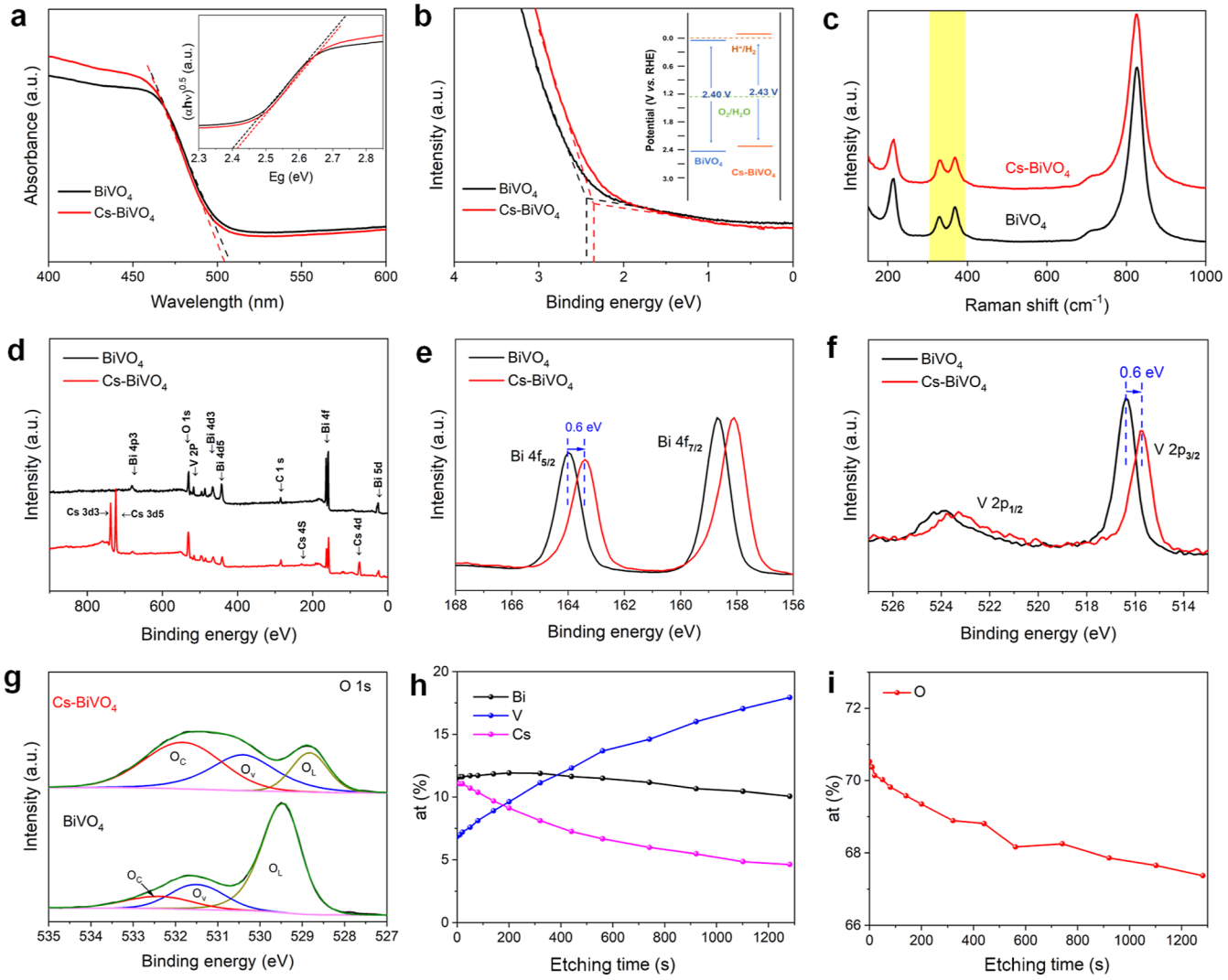

Figure 3. (a) UV−vis diffuse spectra of $BiVO_4$ and Cs-$BiVO_4$ photoanodes. (b) Valence band region for $BiVO_4$ and Cs-$BiVO_4$ photoanodes. (c) Raman spectra of $BiVO_4$ and Cs-$BiVO_4$. (d) XPS survey spectra. (e) Bi 4f, (f) V 2p, and (g) O 1s XPS spectra for bare $BiVO_4$ and Cs-$BiVO_4$ photoanodes. (h) Bi, V, and Cs elements. (i) O element ratio of the Cs-$BiVO_4$ photoanode at different depths.

be due to the fact that $BiVO_4$ photoanodes prepared by different methods are different in morphology, facet exposure, and defects, or due to other factors.[45] Moreover, the photocorrosion of $BiVO_4$ photoanodes during $J-t$ measurements with potassium borate buffer solution is consistent with many other studies where the method used for preparing $BiVO_4$ is the same as that used in our study .[41,46]

Characterization and Formation Mechanism of Cs-$BiVO_4$

To reveal the underlying mechanism of formation of Cs-BiVO, SEM and transmission electron microscopy (TEM) were employed to investigate the morphology and structural changes of Cs-$BiVO_4$. The sharp nano-coral structure of pristine $BiVO_4$ becomes blurry after PEC activation (Figure 2a,b). A similar morphology is not observed in the SEM images of K-$BiVO_4$ and immersion-$BiVO_4$ (Figure S9). A clear amorphous/crystalline heterojunction interface is observed in the TEM images (Figure 2c,d), and it is absent in the TEM image of K-$BiVO_4$ (Figure S10). Fast Fourier transform (FFT) patterns in Figure 2e−g show an amorphous thin layer (~10 nm) on the $BiVO_4$ crystal surface. The line scanning and elemental mapping results from high-angle annular dark-field scanning TEM-energy-dispersive spectroscopy (HAADF-STEM-EDS) reveal that Bi, V, O, and Cs are homogeneously distributed throughout the Cs-$BiVO_4$ region (Figure 2h). A Cs-containing amorphous thin layer is fully covered on the surface of the $BiVO_4$ nano-coral (Figure 2i−m). The SEM and TEM images show that an amorphous thin layer containing Cs^+ is formed on the $BiVO_4$ surface after the Cs^+-dependent PEC-activation.

XRD, UV−vis absorption spectroscopy, ultraviolet photoelectron spectroscopy (UPS), Raman spectroscopy, and X-ray photoelectron spectroscopy (XPS) were employed to further reveal the structure of Cs-$BiVO_4$. Both pristine $BiVO_4$ and Cs-$BiVO_4$ show typical diffraction peaks of monoclinic scheelite $BiVO_4$ (JSPDS no. 14-0688, Figure S11). Besides some intensity changes of the peaks corresponding to the (110) and (011) planes, which are also observed for the other control samples, there are no crucial XRD changes that indicate any unique structural changes of Cs-$BiVO_4$ (Figure S11). The UV−vis absorption spectra of both photoanodes overlap with an absorbance edge of 520 nm, indicating a typical bandgap of 2.40 eV (Figures 3a and S12). The valence band positions of pristine $BiVO_4$ and Cs-$BiVO_4$ were estimated to be 2.43 and 2.32 eV, respectively, by UPS measurements (Figure 3b). The

https://doi.org/10.1021/jacsau.3c00100
JACS Au 2023, 3, 1851−1863

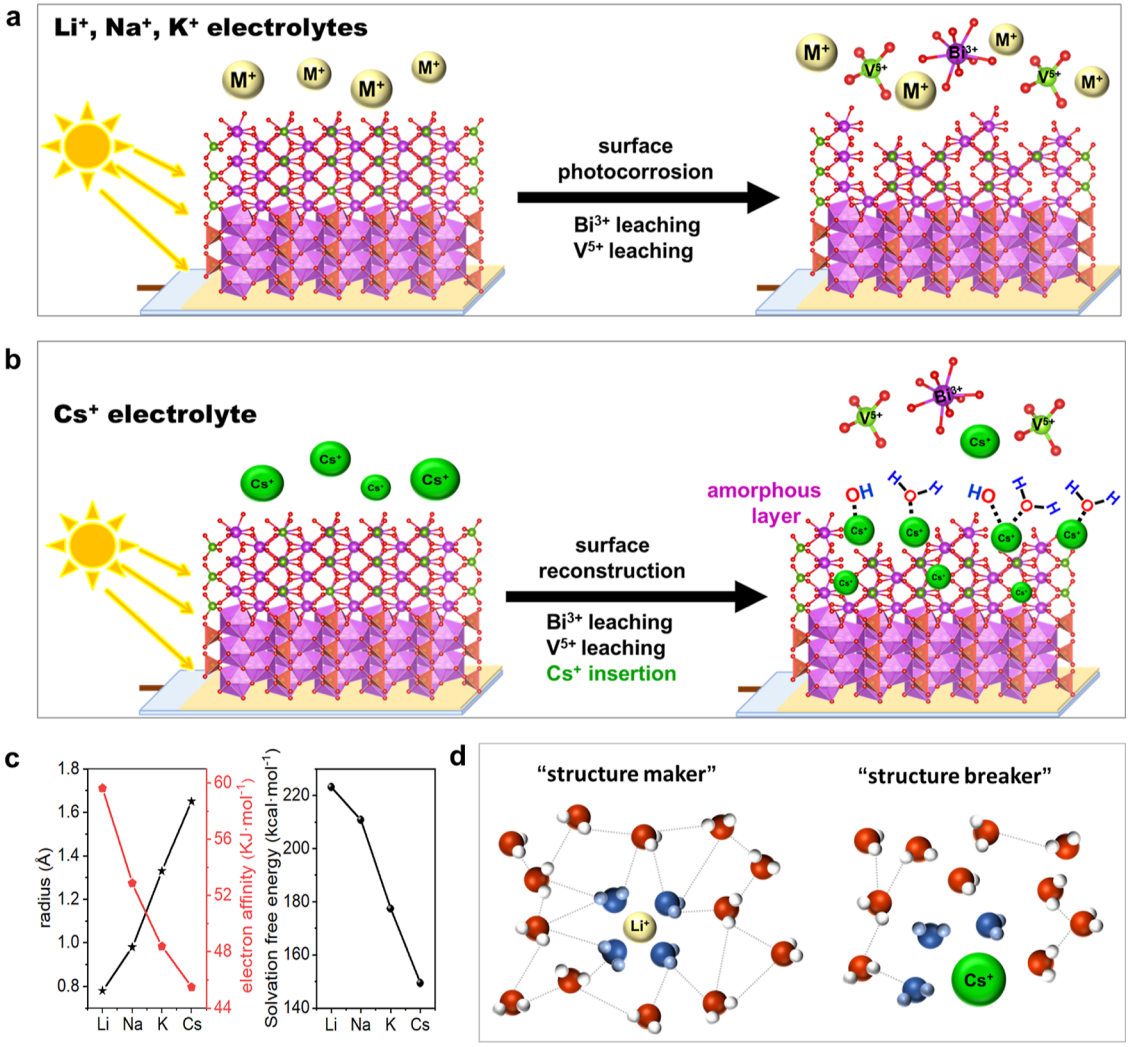

Figure 4. Schematic of the photocorrosion of the $BiVO_4$ surface when an anodic potential is applied under illumination (a) in a buffer solution containing Li^+, Na^+, or K^+, (b) in a buffer solution containing Cs^+. (c) Chemical and physical factors of the alkali metal ions. (d) Schematic of water network structure for water containing different cations.

upshift of the valence band (0.1 eV) can be attributed to the presence of the amorphous thin layer on the surface, as UPS is a surface-sensitive technique. A proposed band−edge diagram is shown in the inset of Figure 3b.

In the Raman spectra, typical peaks at 826, 710, 368, and 330 cm^{-1} are observed for both photoanodes, corresponding to ν_s(V−O), ν_{as}(V−O), $\delta_s(VO_4^{3-})$, and $\delta_{as}(VO_4^{3-})$ vibrations, respectively (Figure 3c).[47] After PEC activation, the $\delta_{as}(VO_4^{3-})$ peak intensity of Cs-$BiVO_4$ at 330 cm^{-1} increases, indicating less symmetric VO_4^{3-} tetrahedra and more asymmetric chemical environment in the Cs-$BiVO_4$ surface layer.[48] In order to confirm that the observed changes in Cs-$BiVO_4$ are unique for Cs-$BiVO_4$, the above spectroscopic studies were also carried out using K-$BiVO_4$ and immersion-$BiVO_4$ photoanodes, and the full comparisons of the pristine $BiVO_4$, Cs-$BiVO_4$, K-$BiVO_4$, and immersion-$BiVO_4$ are shown in Figures S13 and S14.

In the overview of the XPS spectra shown in Figure 3d, in addition to the core-level peaks of Bi (4p, 4d, 4f, and 5d), V (2p), and O (1s), very strong core-level peaks of Cs (3d, 4s, and 4d) are present in Cs-$BiVO_4$, confirming the presence of Cs in the amorphous thin layer. The Cs 3d spectrum shows two splitting peaks at 724.6 and 738.5 eV (Figure S15). The +1 oxidation state of Cs can be indicated by the splitting ΔE(3d) of 13.9 eV. The Bi 4f and V 2p peaks of Cs-$BiVO_4$ both shift about 0.6 eV toward lower binding energy compared to those of pristine $BiVO_4$ (Figure 3e,f). In contrast, the Bi 4f and V 2p peaks of K-$BiVO_4$ and immersion-$BiVO_4$ show a slight shift to the higher binding energy (Figure S16). Such a significant shift (0.6 eV) in Cs-$BiVO_4$ cannot be attributed to local O defects or V vacancies. It is more possible that the amorphous thin layer is a new substance consisting of Cs^+, [BiO_8] units, and [VO_4] units.

This speculation is verified by the O 1s spectrum of Cs-$BiVO_4$ (Figure 3g). Typically, the O 1s spectrum of the pristine $BiVO_4$ is deconvoluted into three fitting peaks: lattice oxygen (O_L, i.e., μ−O of the Bi−O−V moiety) at 529.5 eV, hydroxyl groups bonded to the vacancy environment (O_V, i.e., terminal-OH) at 531.5 eV, and chemisorbed water molecules (O_C, i.e., coordinated H_2O) at 532.4 eV. For Cs-$BiVO_4$, both the O_L and O_V peaks shift about 0.7 eV toward lower binding energy. The intensity of the O_L peak decreases dramatically, indicating the decomposition of the $BiVO_4$ structure. Moreover, the O_C peak of the Cs-$BiVO_4$ shifts to 531.8 eV, and its intensity increases remarkably, indicating abundant coordinated H_2O in the amorphous thin layer. Therefore, the

https://doi.org/10.1021/jacsau.3c00100
JACS Au 2023, 3, 1851−1863

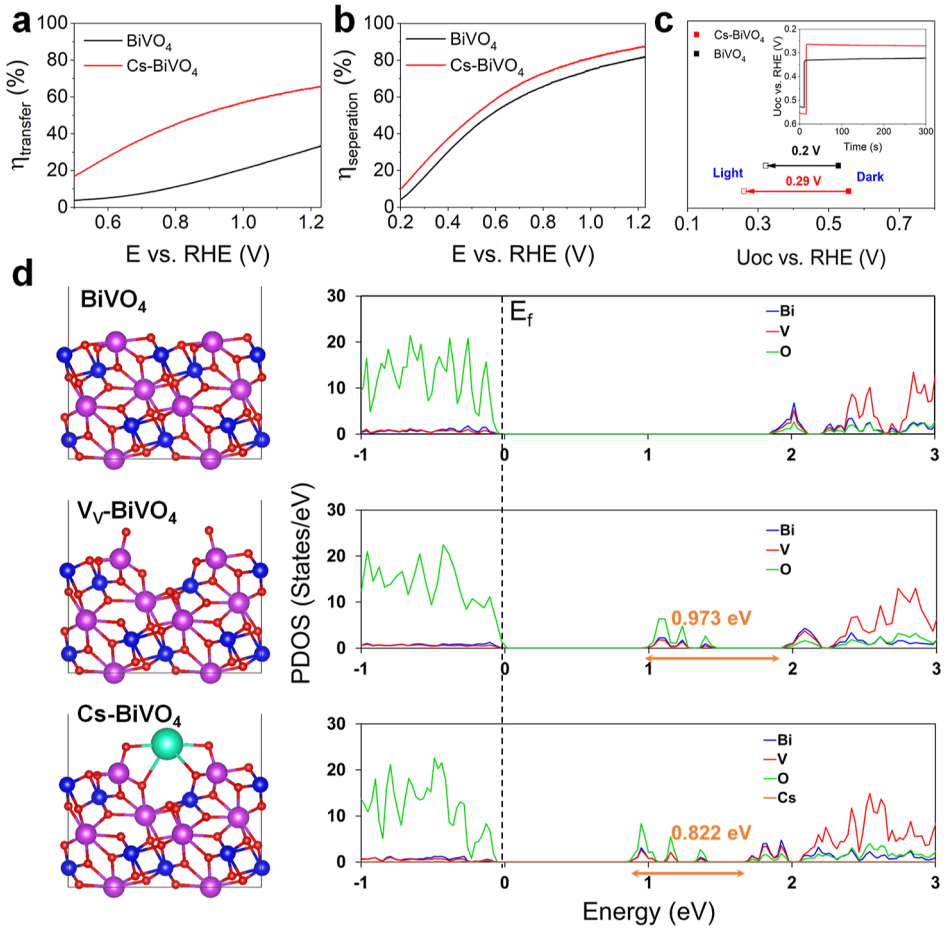

Figure 5. (a) $\eta_{transfer}$ of $BiVO_4$ and Cs-$BiVO_4$ photoanodes. (b) $\eta_{separation}$ of $BiVO_4$ and Cs-$BiVO_4$ photoanodes. (c) U_{OC} of $BiVO_4$ and Cs-$BiVO_4$ photoanodes under dark (solid) and illumination (hollow), and the inset shows the transient photovoltage response within immediate illumination. (d) Optimized structures of $BiVO_4$, V_V-$BiVO_4$, and Cs-$BiVO_4$ and their corresponding PDOS. The values of the width of energy levels from trapped states to CBM (marked in orange) are also illustrated. Violet, blue, red, and cyan represent Bi, V, O, and Cs, respectively.

amorphous thin layer formed on the $BiVO_4$ surface is a Cs^+-doped bismuth vanadium oxide amorphous thin layer (denoted as CsBiVO layer), which contains abundant defects and much more terminal-OH and dangling H_2O in its structure compared to that in pristine $BiVO_4$.

The composition and structure of the CsBiVO layer are further revealed by XPS depth profiles (Figure 3h,i, Table S2). As the etching depth increases, the percentage of Bi element remains unchanged, but the percentage of V element increases from 6.9 to 17.9%, and the percentages of Cs and O decrease from 11.1 and 70.5% to 4.6 and 67.4%, respectively. This indicates that the amorphous thin layer contains a high percentage of Cs^+ and dangling oxygen groups. XPS depth profiles of K-$BiVO_4$ show only trace amounts of K element, which can be attributed to the physical adsorption of K^+ (Table S3). The composition of the CsBiVO layer varies from $Cs_{0.63}Bi_{0.65}V_{0.39}O_4$ on the top surface to $Cs_{0.27}Bi_{0.60}V_{1.06}O_4$ at the inner layers, approaching the theoretical element ratio of $BiVO_4$. This suggests that Cs^+ gradually penetrates the $BiVO_4$ surface during the photocorrosion process. The electrolyte after PEC activation was analyzed by inductively coupled plasma optical emission spectrometry (ICP-OES, Figure S17). The leaching values of both Bi^{3+} and V^{5+} when Cs^+ cations are present in the electrolyte are lower than those obtained when K^+ cations are used. Bi^{3+} and V^{5+} concentrations in the electrolyte show no increase in 5 h of photolysis. Interestingly, the Bi^{3+} concentration starts to decrease after 3 h of photolysis, indicating the protective effect of the CsBiVO layer.

Based on the above studies, Cs^+-dependent PEC activation essentially is a process where a CsBiVO layer develops on the $BiVO_4$ surface via structural reconstruction in the presence of Cs^+. Due to the intrinsically low stability of $BiVO_4$, the leaching of Bi and V ions has been widely observed under different conditions, such as basic treatment[49] and open-circuit photocharging.[50,51] The typical photocorrosion triggers the $BiVO_4$ surface reconstruction, and this phenomenon has attracted more and more attention in this field.[52,53] When an anodic potential is applied under illumination in a buffer solution containing Na^+ and K^+, both Bi^{3+} and V^{5+} leach from the surface, leading to surface corrosion and deactivation of $BiVO_4$ (Figure 4a). However, when Cs^+ cations are present in the electrolyte, Cs^+ participates in the surface photocorrosion reaction to form the CsBiVO layer (Figure 4b). The CsBiVO layer prevents the inner $BiVO_4$ from further photocorrosion and significantly improves the PEC water oxidation performance of $BiVO_4$.

Why Cs-Dependent?

A critical question that needs to be addressed for a complete understanding of the PEC activation surface reconstruction is why the formation of the CsBiVO layer is Cs-dependent. A direct clue is the unique chemical nature of Cs^+ (Table S4).

https://doi.org/10.1021/jacsau.3c00100
JACS Au 2023, 3, 1851−1863

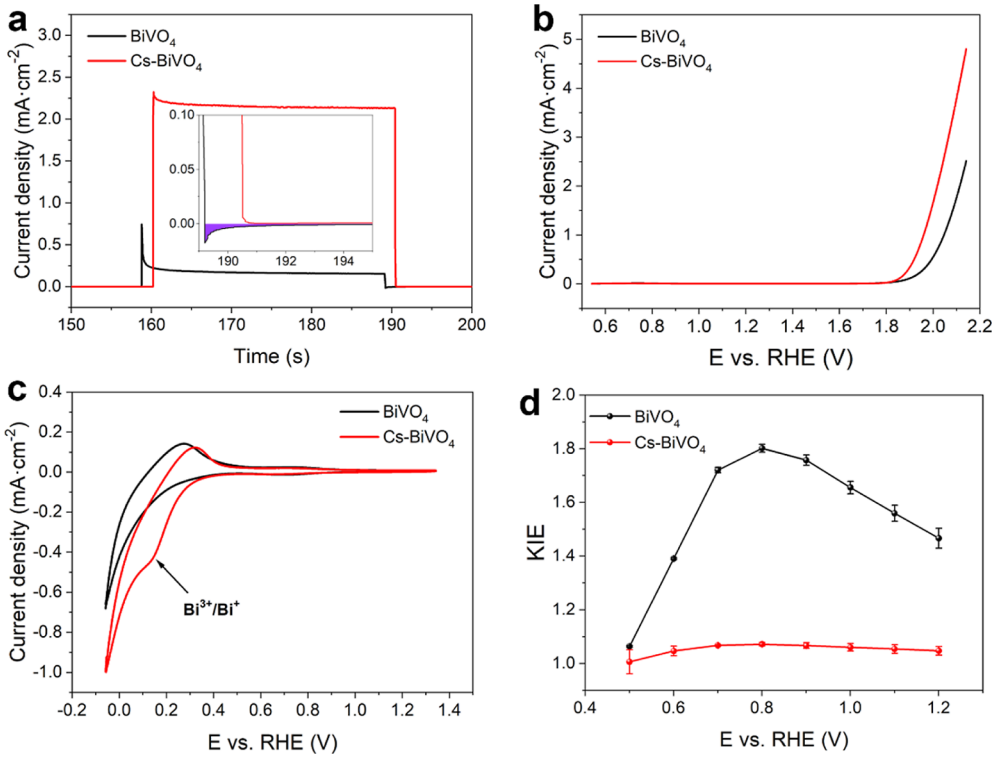

Figure 6. (a) Transient photocurrents measured at 0.8 V_{RHE} for $BiVO_4$ and Cs-$BiVO_4$; the inset shows details of the decay at the moment of shading. (b) LSV cures of $BiVO_4$ and Cs-$BiVO_4$ in the dark at a scan rate of 10 mV s^{-1}. (c) CV cures of $BiVO_4$ and Cs-$BiVO_4$ starting from −0.05 V_{RHE} in the dark at a scan rate of 100 mV s^{-1}. (d) KIE plots of $BiVO_4$ and Cs-$BiVO_4$ were calculated from the photocurrent density ratio in H_2O and D_2O solutions (KIE = J_{H_2O}/J_{D_2O}).

Different cations in the electrolyte solution affect the interfacial water structure and the local pH in the photoanode−electrolyte interface layer. Among the nonradioactive alkali metal cations, Cs^+ has the largest ionic radius, lowest electronegativity, and lowest hydration energy (Figure 4c). The small Li^+ ions with a high charge density can attract H_2O molecules and form a large hydration shell, leading to a more orderly structure than pure H_2O; they are, namely, "structure maker" ions (Figure 4d). In contrast to Li^+, Cs^+ is larger with a lower charge density. It interacts with H_2O molecules weakly, and the H_2O molecules adjacent to Cs^+ are less structured than in pure H_2O; it is, namely, a "structure breaker" ion (Figure 4d).[23] The dissolution of Bi and V ions during PEC photoactivation causes many vacancies on the $BiVO_4$ surface. The desolvation of $Cs^+(H_2O)_n$ is thermodynamically favorable, and the generated Cs^+ in the electric double layer can bind with the O^- groups in the vacancy to gradually form the CsBiVO layer. Although Cs^+ with low hydration energy is a "structure breaker" in the water solution,[23] its large cation radius and suitable electronegativity allow a stable structure in the multiple O^- coordinate environment, leading to the formation of an amorphous thin layer.

DFT calculations were employed to rationalize this interpretation. The impurity formation energies of different alkali metals doped in $BiVO_4$ are shown in Figure S18. The formation energies of Li^+-doped and Na^+-doped $BiVO_4$ are significantly higher than those of K^+-doped and Cs^+-doped $BiVO_4$, indicating that large K^+ and Cs^+ are more energetically favorable to form an alkali-metal cation-doped amorphous layer. Because the structure of the CsBiVO layer cannot be well-defined, it is difficult to perform more accurate simulations. However, this result qualitatively verifies that the unique chemical nature of Cs^+ is essential for the formation of the CsBiVO amorphous layer.

Implications on the Cs-$BiVO_4$ PEC Performance

PEC kinetics of the Cs-$BiVO_4$ photoanodes were investigated to reveal the promotional effect of the CsBiVO layer. Like most post-treatment-derived $BiVO_4$,[43,44,54] the J_{abs} (photocurrent density at 100% internal quantum efficiency) of the Cs-$BiVO_4$ shows no marked changes, consistent with unchanged band gap determined by the UV−vis spectrum (Figure S12). Charge separation efficiency in the bulk (η_{sep}) and charge transfer efficiency at the semiconductor/electrolyte interface (η_{trans}) were evaluated separately using Na_2SO_3 as a hole scavenger (Figure S19). The η_{trans} value of the Cs-$BiVO_4$ increases 1.8−2.5 times compared to that of pristine $BiVO_4$ (Figure 5a); however, the enhancement of the η_{sep} value is less than 7% on average (Figure 5b). This indicates that the PEC performance improvement is mainly attributed to the dramatic acceleration of the interfacial charge injection.

The influence of the CsBiVO layer on carrier lifetime was studied at different timescales. In the nanosecond transient absorption spectra, which represent the carrier state in the bulk, the decay kinetics of the pristine $BiVO_4$ and Cs-$BiVO_4$ are comparable (Figure S20), consistent with the small change in η_{sep}. The subsequent hole injection processes were monitored by electrochemical impedance spectroscopy (EIS) and open-circuit voltage (U_{OC}). The measured interfacial charge transfer resistance (R_{ct}) of Cs-$BiVO_4$ is much smaller than that of pristine $BiVO_4$ (Figure S21), indicating improved carrier transfer and water oxidation rate at the solid−liquid interface. The ΔU_{OC} value of Cs-$BiVO_4$ after light-on is 90 mV higher than that of bare $BiVO_4$ (Figure 5c). The higher

https://doi.org/10.1021/jacsau.3c00100
JACS Au 2023, 3, 1851−1863

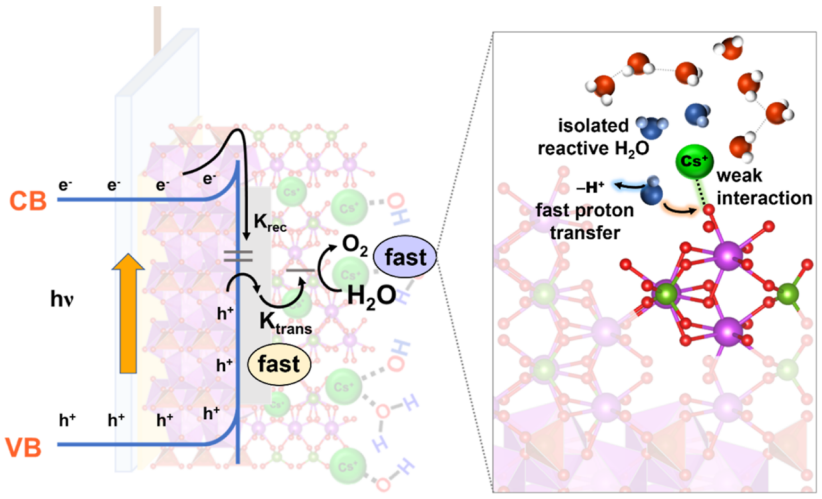

Figure 7. Illustration of the proposed mechanism for the PEC performance promotion of Cs-$BiVO_4$ due to the CsBiVO amorphous thin layer.

photovoltage of Cs-$BiVO_4$ provides a stronger driving force to inject the photogenerated holes into electrolytes for water oxidation.

To deeply understand the changes in carrier transfer, the electronic band structures of $BiVO_4$, $BiVO_4$ with vanadium vacancy (V_V-$BiVO_4$), and the proposed Cs-$BiVO_4$ local structure were explored by calculating the projected density of states (PDOS). Figure 5d shows that the valence band maximum is mainly composed of O atomic orbitals, while the conduction band minimum (CBM) is composed of V and O atomic orbitals, consistent with the previous reports.[55,56] Compared with pristine $BiVO_4$, a new energy level is present between the band gap of V_V-$BiVO_4$. This new energy level formed by the hybridization of O, V, and Bi orbitals is supposed to be an electron−hole recombination center, leading to low charge transfer efficiency and decreased PEC performance.[57,58] However, with the introduction of Cs dopant into the V vacancy, the energy width of the energy level to CBM is reduced from 0.973 to 0.822 eV. The mediate energy level of Cs-$BiVO_4$ closer to the conduction band may serve as electron donor states, which increases the extraction of holes from the $BiVO_4$ bulk to the CsBiVO layer.[59]

Surface water oxidation is the final step in determining η_{trans}. One way to assess the rate of surface water oxidation is to measure the spike of the transient photocurrent, which is caused by the discrepancy between fast carrier generation and slow surface water oxidation. When the light is turned on, the photocurrent spike in Cs-$BiVO_4$ is distinctly smaller than that in pristine $BiVO_4$ (Figure 6a). During the light-off period, the accumulated charges of the pristine $BiVO_4$ counted based on the integration of the damped-current curve was 0.013 mC; however, no charge accumulation is observed for Cs-$BiVO_4$ (inset in Figure 6a). The transient photocurrent behavior indicates that Cs-$BiVO_4$ distinctly increases the surface water oxidation rate.

The acceleration of the surface water oxidation was confirmed by electrochemical water oxidation in the dark. Linear sweep voltammetry (LSV) curves for water oxidation show the superior water-oxidation performance of the CsBiVO layer, with an approximately 100 mV cathodic shift of the onset potential and an approximately twofold increase in the catalytic current density (Figure 6b). The outstanding water oxidation activity of the CsBiVO layer is due to its highly disordered structure (more Bi^{3+} active sites, O_V, and coordinated H_2O). The Bi^{3+} active sites can be identified by the unique Bi^{3+}/Bi^+ redox peak at 0.15 V_{RHE} in the cyclic voltammetry (CV) curves of Cs-$BiVO_4$ (Figure 6c). In the CV scans from 2.15 to −0.05 V_{RHE}, a sharp water-oxidation catalytic peak and a Bi^{3+}/Bi^+ redox peak are detected; however, both vanish from the second and subsequent scans from 2.15 to −0.05 V_{RHE} (Figure S22a). The photocurrent density of the reduced Cs-$BiVO_4$ that underwent a low potential scan decreased significantly (Figure S22b). In contrast, the high catalytic peak remains steady during the CV sweeps from 0.45 to 2.15 V_{RHE} (Figure S23). The increase in the electrochemically active surface area (ECSA) caused by morphological changes may contribute to water oxidation catalysis, but the effect is minor because the ECSA of the Cs-$BiVO_4$ photoanode, after losing its high catalytic performance, remains unchanged (Figure S24).

In addition to the increase of Bi^{3+} active sites, the fast surface water oxidation of the Cs-$BiVO_4$ is also owing to the existence of Cs^+ in the CsBiVO layer.[28,30−36] The "structure breaker" Cs^+ with unique electronegativity and ionic radius changes the interfacial H_2O net structure, generating more isolated reactive H_2O and OH^- and assisting proton-coupled electron transfer (PCET). At the same time, the low Lewis acidity of Cs^+ also influences the reactivity of the high-valent bismuth-oxo intermediate to facilitate O−O bond formation. These effects can be demonstrated by deuterium kinetic isotope experiments. Kinetic isotope effects (KIE) of Cs-$BiVO_4$ and $BiVO_4$ were determined by the $J-V$ curves of Cs-$BiVO_4$ and pristine $BiVO_4$ in H_2O and D_2O (Figure S25). The KIE values for Cs-$BiVO_4$ and $BiVO_4$ are 1.06 and 1.80 at 0.8 V_{RHE}, respectively (Figure 6d). The obvious decrease in KIE indicates that the catalytic mechanism of the water oxidation of Cs-$BiVO_4$ has changed, and proton transfer is no longer involved in the rate-determining step.

Based on the above PEC kinetics and dark electrochemical studies, a complete mechanism is proposed in Figure 7 for the PEC performance promotion. The CsBiVO amorphous thin layer has two functions: (i) improving carrier transfer by efficient hole extraction and storage and (ii) acting as an efficient water-oxidation catalyst layer with abundant Bi^{3+} active sites and Cs^+ effects. Cs^+ is essential in forming the CsBiVO layer, and it also similarly accelerates water oxidation as Ca^{2+} in the Mn_4CaO_5 OEC, i.e., providing reactive H_2O,

https://doi.org/10.1021/jacsau.3c00100
JACS Au 2023, 3, 1851−1863

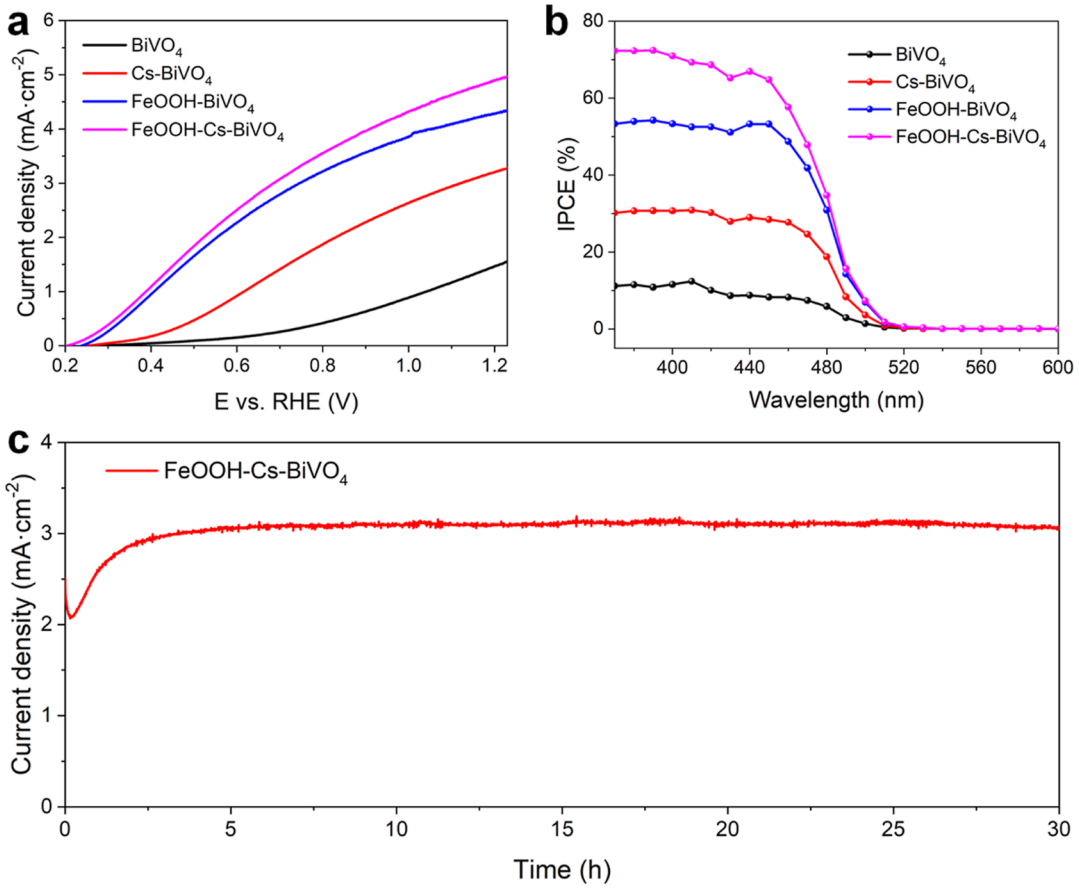

Figure 8. (a) $J-V$ curves of pristine $BiVO_4$, Cs-$BiVO_4$, FeOOH-$BiVO_4$, and FeOOH-Cs-$BiVO_4$ photoanodes. (b) IPCEs of $BiVO_4$, Cs-$BiVO_4$, FeOOH-$BiVO_4$, and FeOOH-Cs-$BiVO_4$ photoanodes at 0.8 V_{RHE}. (c) $J-t$ curves of FeOOH-Cs-$BiVO_4$ photoanodes measured at 0.8 V_{RHE}. Measurements of (a) and (b) were performed in 1.0 M potassium borate buffer (pH 9.5) under AM 1.5 G simulated sunlight (100 mW cm^{-2}) at a scan rate of 10 mV s^{-1}. Measurement of (c) was performed in 1.0 M cesium borate buffer (pH 9.5).

adjusting the reactivity of high-valent Mn-oxo, and promoting PCET.[60,61]

Benchmark PEC Water Splitting with Modification of FeOOH Cocatalyst

The Cs-$BiVO_4$ photoanode loaded with cocatalysts also showed obvious advantages over the pristine $BiVO_4$ photoanode treated with the same procedure. On modifying the Cs-$BiVO_4$ photoanode with the FeOOH cocatalyst layer,[62] the photocurrent for water oxidation reached 5.1 mA cm^{-2} at 1.23 V_{RHE} (Figure 8a). In contrast, the FeOOH-deposited pristine $BiVO_4$ showed a photocurrent of 4.5 mA cm^{-2}. Accordingly, the maximum IPCE value of FeOOH-Cs-$BiVO_4$ is determined high to ∼70% at a wavelength of about 400 nm (Figure 8b). Moreover, the FeOOH-Cs-$BiVO_4$ photoanode exhibits very good stability. A steady photocurrent over 3.0 mA cm^{-2} at 0.8 V_{RHE} lasted for 30 h without an obvious decrease (Figure 8c). The PEC performance comparisons of FeOOH-Cs-$BiVO_4$ with reported benchmark $BiVO_4$ photoanodes are listed in Table S5.

In summary, we report, for the first time, the Cs^+-dependent surface reconstruction and passivation of $BiVO_4$ photoanodes, which dramatically enhanced PEC water oxidation. Benchmark PEC water splitting is achieved for both cocatalyst-free (3.3 mA cm^{-2} at 1.23 V_{RHE}) and cocatalyst-modified Cs-$BiVO_4$ (5.1 mA cm^{-2} at 1.23 V_{RHE}). The functional CsBiVO layer formed via Cs^+-dependent surface reconstruction of $BiVO_4$ is the underlying mechanism for the PEC activation, and the "structure breaker" nature of Cs^+ is the fundamental factor for this phenomenon. We believe that this work reveals a new strategy to improve the catalytic activity and stability of water oxidation photoanodes. Moreover, results obtained from this work extend the understanding of the Cs^+ chemistry and the effects of redox-inert cations in electrochemical and PEC reactions.

METHODS

Materials

The materials included bismuth nitrate pentahydrate [$Bi(NO_3)_3 \cdot 5H_2O$, 99%], *p*-benzoquinone (98%), potassium iodide (KI, 99%), vanadyl acetylacetonate [$VO(acac)_2$, 98%], cesium hydroxide monohydrate (CsOH, 99%), boric acid (H_3BO_3, 99.8%), lithium hydroxide monohydrate (LiOH, 99%), sodium hydroxide (NaOH, 99%), potassium hydroxide (KOH, 99%), sodium sulfite (Na_2SO_3, 98%), nitric acid solution (HNO_3, 70%), ethanol absolute (EtOH, 99.7%), dimethyl sulfoxide (DMSO, 99.7%), and deuterium oxide (D_2O, 99.9%D). Ultra-pure water (18.2 MΩ·cm^{-1}) supplied by a Milli-Q system (Merck Millipore) was used in all experiments. Fluorine-doped tin oxide (FTO)-coated glass substrates were purchased from Pilkington (∼14 Ω·cm^{-2}) and were successively cleaned in Milli-Q water, ethanol, and acetone by an ultrasonic bath.

Preparation of $BiVO_4$ Photoanodes

The nano-porous $BiVO_4$ photoanodes were prepared according to a reported method with some modifications.[63] In brief, 0.04 M $Bi(NO_3)_3$ was dissolved into 50 mL of pH 1.7 HNO_3 aqueous solution and sonicated for several minutes. Then, 0.4 M KI was added

https://doi.org/10.1021/jacsau.3c00100
JACS Au 2023, 3, 1851−1863

to this solution with a further 5 min sonification. Afterward, 20 mL of ethanol containing 0.23 M *p*-benzoquinone was mixed with the above solution with vigorous stirring. The electrodeposition of the BiOI precursor was carried out at −0.1 V vs Ag/AgCl for 3 min at room temperature, using a typical three-electrode cell: an FTO working electrode (WE), a saturated Ag/AgCl reference electrode (RE), and a platinum wire counter electrode (CE). The BiOI electrodes were washed thoroughly with Milli-Q water and dried at room temperature. To convert BiOI to $BiVO_4$, about 25 μL of DMSO solution containing 0.4 M $VO(acac)_2$ was dropped onto the BiOI electrode (1 cm × 1 cm) surface and then annealed at 450 °C for 2 h in a muffle furnace (KSL-1100X-S, Kejing). Finally, residual V_2O_5 on the $BiVO_4$ electrodes was removed by soaking them in 1 M NaOH solution for 20 min. The resulting bare $BiVO_4$ electrodes were washed thoroughly with Milli-Q water and dried at room temperature.

Preparation of SILAR-$BiVO_4$ Photoanodes

The SILAR-$BiVO_4$ photoanodes were prepared according to a reported method with some modifications.[42] First, a piece of FTO was vertically immersed in a 5 mM Bi $(NO_3)_3$ solution for 10 s and then immersed in a 5 mM KI solution for 10 s; this process was repeated 20 times to obtain the BiOI electrodes. Next, to convert BiOI to $BiVO_4$, about 25 μL of DMSO solution containing 0.4 M $VO(acac)_2$ was dropped onto the BiOI electrode surface and then annealed at 500 °C for 2 h in a muffle furnace (KSL-1100X-S, Kejing). Finally, residual V_2O_5 on the $BiVO_4$ surface was removed by soaking them in 1 M NaOH solution for 20 min. The resulting $BiVO_4$ electrodes were washed with Milli-Q water and dried at room temperature.

Preparation of Cs-$BiVO_4$ Photoanodes

Cs^+ ion modification of the $BiVO_4$ photoanode was performed by simple photo-polarization in a 1.0 M cesium borate buffer solution (pH 9.5) with 0.8 V_{RHE} bias. Then, the treated $BiVO_4$ electrode was removed from the electrolyte and rinsed with Milli-Q water. (The 1.0 M cesium borate buffer, prepared by adjusting the pH of 1.0 M H_3BO_3 solution to 9.5 with CsOH, was used as the electrolyte.) Li-$BiVO_4$, Na-$BiVO_4$, and K-$BiVO_4$ were treated with a similar method in 1.0 M lithium borate, sodium borate, and potassium borate, respectively.

Preparation of FeOOH-Cs-$BiVO_4$ and FeOOH-$BiVO_4$ Photoanodes

FeOOH was deposited from an aqueous 0.1 M $FeSO_4$ solution via a PEC-assisted deposition,[62] under 1 sun AM 1.5 G irradiation, at a constant potential of 0.25 V vs Ag/AgCl for 17 min (equivalent to passing a total charge of ∼45 mC cm^{-2}). Before the photo-deposition of FeOOH, the solution was purged with nitrogen gas for 30 min.

Physical Characterization

The crystalline structure was identified by XRD (D8 Advance, Bruker) using Cu Kα radiation at 40 kV and 40 mA. SEM and TEM were performed using Regulus 8230, Hitachi and Talos L120C G2, Thermo Fisher Scientific. UV−visible diffuse reflectance spectra were recorded on a UV-2700 (Shimadzu) spectrometer by using $BaSO_4$ as the reference. Raman spectra were collected using a Raman spectrometer (Alpha300RAS, WITec). The time-resolved transient absorption (TA) spectra were recorded on an LP980 spectrometer (Edinburgh Instruments Ltd., model LP980), combined with a compact Q-switched Nd: YAG laser (Continuum). The element content was determined by inductively coupled plasma mass spectroscopy (iCAP RQ, Thermo Fisher Scientific).

The elemental composition was determined by XPS (ESCALAB 250xi, Thermo Fisher Scientific). To minimize the effects of charging at the films, the charge compensation gun was used for charge neutralization. The binding energies were calibrated with respect to the residual C 1s peak at 284.8 eV. For depth profiling, Ar^+ ion with 1 keV energy was used to etch a 3.25 mm × 3.25 mm area of the sample at an angle of 40° to the surface normal. At the beginning of the profile, XPS measurements were performed after every 10 s of sputtering, while the profiling of the bulk was performed with a longer sputtering cycle. The change in the element content can be noticed from the change of peak area at different sputtering times. All the samples were carefully rinsed with ultrapure water (18.2 MΩ) and were kept in a sealed sample box to avoid surface contamination.

Electrochemical and PEC Characterization

All PEC measurements were performed in a standard three-electrode system with an electrochemical analyzer (CHI660E). The $BiVO_4$ photoanodes, a saturated Ag/AgCl (0.197 V vs NHE), and a Pt wire mesh were configured as WE, RE, and CE, respectively. The light source was a 100 W Xenon arc lamp with an AM 1.5G filter (100 mW cm^{-2}, PLS-FX300HU, perfect light) to gain simulated AM 1.5G solar illumination. All $BiVO_4$ photoanodes were illuminated from the back side, and the illuminated areas were 1 cm^2. 1 M KBi with or without 0.2 M sodium sulfite (Na_2SO_3) as a hole scavenger was used as the electrolyte. Linear scan voltammetry (LSV) with a scan rate of 10 mV s^{-1} was used for the photocurrent measurements by scanning the potential from −0.6 to 0.6 V vs Ag/AgCl. The measured potential was converted into a potential with respect to a reversible hydrogen electrode (RHE) according to the Nernst equation ($E_{RHE} = E_{Ag/AgCl} + 0.197 + 0.059 \times pH$).

For EIS measurements, a sinusoidal voltage pulse of 10 mV amplitude was applied on a bias voltage of 0.8 V_{RHE} with frequencies ranging from 100 kHz to 0.01 Hz. The ABPEs of $BiVO_4$ photoanodes were calculated from the *J*−*V* curves according to the equation: ABPE (%) = $(J_{light} - J_{dark}) \times (1.23 - V_{RHE})/P_{light} \times 100\%$. Incident light-electron conversion efficiency (IPCE) was measured at 0.8 V_{RHE} in 1 M KBi using zanher, Zennium pro. The photostability test is carried out in 0.8 V_{RHE} in 1 M KBi (pH 9.5) solution under AM 1.5 G solar illumination. The Faradaic efficiency was calculated according to the equation: FE (%) = O_2(actual)/O_2(theoretical) × 100%. Charge separation efficiency in the bulk (η_{sep}) and charge transfer efficiency at the semiconductor/electrolyte interface (η_{trans}) of $BiVO_4$ and Cs-$BiVO_4$ photoanodes were calculated using the following equation

$$\eta_{transfer} = J_{water}/J_{sulfite}$$

$$\eta_{sep} = J_{Na_2SO_3}/J_{abs}$$

Computational Details

All the spin-polarized calculations based on DFT in the work were carried out using the Vienna Ab initio Simulation program (VASP).[64,65] The core−electron interactions were described by the projector-augmented wave (PAW) method,[65,66] while the plane-wave basis expansion cutoff energy was set to be 450 eV. The exchange and correlation functional was calculated by the generalized gradient approximation (GGA) with Perdew−Burke−Ernzerhof (PBE).[67] The strong-correlated corrections were considered by the GGA + *U* method with a *U*−*J* value of 2.7 eV for V 3d states.[55,68,69] Equilibrium was reached when the forces on the relaxed atoms and the energies in the self-consistent iterations became less than 0.05 eV/Å and 10^{-5} eV, respectively. The van der Waals (vdW) interaction was described by the DFT-D3 method.[70,71] The monoclinic $BiVO_4$ structure with calculated lattice parameters of *a* = 5.063 Å, *b* = 5.285 Å, *c* = 11.943 Å, and the 2.41 eV band gap are consistent with the literature.[72−74] A vacuum height of 15 Å was used to eliminate the interaction between neighboring slabs. For the model construction, a $p(1 \times 1)$ $BiVO_4$ (110) surface with four layers was modeled, with the top two layers fully relaxed and the bottom two layers kept fixed to mimic the bulk region. The doped structure was built by replacing one V atom in the top layer by Li, Na, K, Rb, or Cs. The Monkhorst−Pack mesh k-point was set to (4 × 2 × 1) for all the systems. The impurity formation energy ($E_{formation}$) was calculated by the formula as follows

$$E_{formation} = E_{tot}[BiV_{1-x}M_xO_4] - E_{tot}[BiVO_4] - E[M] + \mu_V$$

where $E_{tot}[BiV_{1-x}M_xO_4]$ (M = Li, Na, K, Rb, Cs) and $E_{tot}[BiVO_4]$ are the total energy of the doped $BiV_{1-x}M_xO_4$ and the pristine $BiVO_4$, respectively. $E[M]$ and μ_V are the energy per atom in bulk metal and the chemical potential of V, respectively.

https://doi.org/10.1021/jacsau.3c00100
JACS Au 2023, 3, 1851−1863

■ ASSOCIATED CONTENT

Supporting Information

The Supporting Information is available free of charge at https://pubs.acs.org/doi/10.1021/jacsau.3c00100.

Physical characterization, including SEM data, XPS data, XRD data, UPS data, Raman data, and ICP−MS data and additional $J-V$ curves, $J-t$ curves, cyclic voltammograms, and other data as noted in the text (PDF)

■ AUTHOR INFORMATION

Corresponding Authors

Yi Jiang − *College of Chemistry, Liaoning University, Shenyang 110036 Liaoning, China;* orcid.org/0000-0002-6266-7615; Email: jiangyi@lnu.edu.cn

Biaobiao Zhang − *Center of Artificial Photosynthesis for Solar Fuels and Department of Chemistry, School of Science and Research Center for Industries of the Future, Westlake University, Hangzhou 310024 Zhejiang, China; Institute of Natural Sciences, Westlake Institute for Advanced Study, Hangzhou 310024 Zhejiang, China;* orcid.org/0000-0002-4093-1251; Email: zhangbiaobiao@westlake.edu.cn

Authors

Chen Tao − *College of Chemistry, Liaoning University, Shenyang 110036 Liaoning, China*

Yunxuan Ding − *Center of Artificial Photosynthesis for Solar Fuels and Department of Chemistry, School of Science and Research Center for Industries of the Future, Westlake University, Hangzhou 310024 Zhejiang, China; Institute of Natural Sciences, Westlake Institute for Advanced Study, Hangzhou 310024 Zhejiang, China*

Bingquan Jia − *Center of Artificial Photosynthesis for Solar Fuels and Department of Chemistry, School of Science and Research Center for Industries of the Future, Westlake University, Hangzhou 310024 Zhejiang, China; Institute of Natural Sciences, Westlake Institute for Advanced Study, Hangzhou 310024 Zhejiang, China*

Ruitong Liu − *Center of Artificial Photosynthesis for Solar Fuels and Department of Chemistry, School of Science and Research Center for Industries of the Future, Westlake University, Hangzhou 310024 Zhejiang, China*

Peifeng Li − *Center of Artificial Photosynthesis for Solar Fuels and Department of Chemistry, School of Science and Research Center for Industries of the Future, Westlake University, Hangzhou 310024 Zhejiang, China*

Wenxing Yang − *Center of Artificial Photosynthesis for Solar Fuels and Department of Chemistry, School of Science and Research Center for Industries of the Future, Westlake University, Hangzhou 310024 Zhejiang, China; Institute of Natural Sciences, Westlake Institute for Advanced Study, Hangzhou 310024 Zhejiang, China*

Lixin Xia − *College of Chemistry, Liaoning University, Shenyang 110036 Liaoning, China*

Licheng Sun − *Center of Artificial Photosynthesis for Solar Fuels and Department of Chemistry, School of Science and Research Center for Industries of the Future, Westlake University, Hangzhou 310024 Zhejiang, China; Institute of Natural Sciences, Westlake Institute for Advanced Study, Hangzhou 310024 Zhejiang, China*

Complete contact information is available at: https://pubs.acs.org/10.1021/jacsau.3c00100

Author Contributions

C. Tao: materials synthesis, photoelectrochemical tests, results analysis, and writing the original draft. Y. Ding: theoretical computations. B. Jia and P. Li: SEM, TEM, and XPS characterization. R. Liu and W. Yang: time-resolved transient absorption spectroscopy. Y. Jiang and B. Zhang: experimental design, supervision, revision and editing of the manuscript, funding acquisition, and project administration. L. Sun and L. Xia: supervision and funding acquisition. All authors participated in discussions and manuscript proofreading. CRediT: **Chen Tao** data curation, formal analysis, investigation, methodology, writing-original draft; **Yi Jiang** conceptualization, funding acquisition, resources, supervision; **Yunxuan Ding** data curation, investigation, software; **Bingquan Jia** data curation, investigation; **Ruitong Liu** data curation, investigation; **Peifeng Li** data curation, formal analysis, investigation; **Wenxing Yang** formal analysis, funding acquisition, investigation, resources; **Lixin Xia** methodology, resources, supervision; **Licheng Sun** funding acquisition, resources, supervision; **Biaobiao Zhang** conceptualization, funding acquisition, investigation, methodology, resources, supervision, writing-original draft, writing-review & editing.

Notes

The authors declare no competing financial interest.

■ ACKNOWLEDGMENTS

This work is financially supported by the National Key R&D Program of China (2022YFC3401802, to B.Z.), the National Natural Science Foundation of China (22279105, to B.Z.; 22179056, to Y.J.), the starting-up package from Westlake University (to B.Z., W.Y., and L.S.), the Kunpeng research fund from Zhejiang Province (to L.S.), Research Center for Industries of The Future, and Zhejiang Baima Lake Laboratory. We thank the Center of Artificial Photosynthesis (CAP) for Solar Fuels at Westlake University for academic and instrument support. We thank Westlake University HPC Center for computation support. We thank the Instrumentation and Service Center for Physical Sciences (ISCPS) and the Instrumentation and Service Center for Molecular Sciences (ISCMS) at Westlake University for the facility support and technical assistance. We thank Dr. Pei Sheng for the XPS experiments and discussions.

■ DEDICATION

This paper is dedicated to Prof. Licheng Sun on the occasion of his 60th birthday.

■ REFERENCES

(1) Abdi, F. F.; Savenije, T. J.; May, M. M.; Dam, B.; van de Krol, R. The origin of slow carrier transport in $BiVO_4$ thin film photoanodes: a time-resolved microwave conductivity study. *J. Phys. Chem. Lett.* **2013**, *4*, 2752−2757.

(2) Qiu, Y.; Liu, W.; Chen, W.; Chen, W.; Zhou, G.; Hsu, P. C.; Zhang, R.; Liang, Z.; Fan, S.; Zhang, Y.; et al. Efficient solar-driven water splitting by nanocone $BiVO_4$-perovskite tandem cells. *Sci. Adv.* **2016**, *2*, No. e1501764.

(3) Ye, K. H.; Li, H.; Huang, D.; Xiao, S.; Qiu, W.; Li, M.; Hu, Y.; Mai, W.; Ji, H.; Yang, S. Enhancing photoelectrochemical water splitting by combining work function tuning and heterojunction engineering. *Nat. Commun.* **2019**, *10*, 3687.

(4) Zhang, K.; Jin, B.; Park, C.; Cho, Y.; Song, X.; Shi, X.; Zhang, S.; Kim, W.; Zeng, H.; Park, J. H. Black phosphorene as a hole extraction

layer boosting solar water splitting of oxygen evolution catalysts. *Nat. Commun.* **2019**, *10*, 2001.
(5) Zhang, W.; Tian, M.; Jiao, H.; Jiang, H.-Y.; Tang, J. Conformal $BiVO_4/WO_3$ nanobowl array photoanode for efficient photoelectrochemical water splitting. *Chin. J. Catal.* **2022**, *43*, 2321−2331.
(6) Luo, W.; Li, Z.; Yu, T.; Zou, Z. Effects of surface electrochemical pretreatment on the photoelectrochemical performance of Mo-doped $BiVO_4$. *J. Phys. Chem. C* **2012**, *116*, 5076−5081.
(7) Ye, H.; Park, H. S.; Bard, A. J. Screening of electrocatalysts for photoelectrochemical water oxidation on W-doped $BiVO_4$ photocatalysts by scanning electrochemical microscopy. *J. Phys. Chem. C* **2011**, *115*, 12464−12470.
(8) Li, D.; Liu, Y.; Shi, W.; Shao, C.; Wang, S.; Ding, C.; Liu, T.; Fan, F.; Shi, J.; Li, C. Crystallographic-orientation-dependent charge separation of $BiVO_4$ for solar water oxidation. *ACS Energy Lett.* **2019**, *4*, 825−831.
(9) Han, H. S.; Shin, S.; Kim, D. H.; Park, I. J.; Kim, J. S.; Huang, P.-S.; Lee, J.-K.; Cho, I. S.; Zheng, X. Boosting the solar water oxidation performance of a $BiVO_4$ photoanode by crystallographic orientation control. *Energy Environ. Sci.* **2018**, *11*, 1299−1306.
(10) Wang, Y.; Li, F.; Zhou, X.; Yu, F.; Du, J.; Bai, L.; Sun, L. Highly efficient photoelectrochemical water splitting with an immobilized molecular Co_4O_4 cubane catalyst. *Angew. Chem., Int. Ed.* **2017**, *56*, 6911−6915.
(11) Zhou, Z.; Chen, J.; Wang, Q.; Jiang, X.; Shen, Y. Enhanced photoelectrochemical water splitting using a cobalt-sulfide-decorated $BiVO_4$ photoanode. *Chin. J. Catal.* **2022**, *43*, 433−441.
(12) Xu, C.; Sun, W.; Dong, Y.; Dong, C.; Hu, Q.; Ma, B.; Ding, Y. A graphene oxide−molecular Cu porphyrin-integrated $BiVO_4$ photoanode for improved photoelectrochemical water oxidation performance. *J. Mater. Chem. A* **2020**, *8*, 4062−4072.
(13) Cao, X.; Xu, C.; Liang, X.; Ma, J.; Yue, M.; Ding, Y. Rationally designed/assembled hybrid $BiVO_4$-based photoanode for enhanced photoelectrochemical performance. *Appl. Catal., B* **2020**, *260*, 118136.
(14) Yin, J.; Hu, Y.; Yoon, J. Fluorescent probes and bioimaging: alkali metals, alkaline earth metals and pH. *Chem. Soc. Rev.* **2015**, *44*, 4619−4644.
(15) Saveleva, V. A.; Wang, L.; Kasian, O.; Batuk, M.; Hadermann, J.; Gallet, J. J.; Bournel, F.; Alonso-Vante, N.; Ozouf, G.; Beauger, C.; Mayrhofer, K. J. J.; Cherevko, S.; Gago, A. S.; Friedrich, K. A.; Zafeiratos, S.; Savinova, E. R. Insight into the Mechanisms of High Activity and Stability of Iridium Supported on Antimony-Doped Tin Oxide Aerogel for Anodes of Proton Exchange Membrane Water Electrolyzers. *ACS Catal.* **2020**, *10*, 2508−2516.
(16) Leonard, N. G.; Chantarojsiri, T.; Ziller, J. W.; Yang, J. Y. Cationic Effects on the Net Hydrogen Atom Bond Dissociation Free Energy of High-Valent Manganese Imido Complexes. *J. Am. Chem. Soc.* **2022**, *144*, 1503−1508.
(17) Yocum, C. F. The calcium and chloride requirements of the O_2 evolving complex. *Coord. Chem. Rev.* **2008**, *252*, 296−305.
(18) Fukuzumi, S.; Ohtsu, H.; Ohkubo, K.; Itoh, S.; Imahori, H. Formation of superoxide−metal ion complexes and the electron transfer catalysis. *Coord. Chem. Rev.* **2002**, *226*, 71−80.
(19) Fukuzumi, S.; Ohkubo, K.; Lee, Y.; Nam, W. Lewis acid coupled electron transfer of metal-oxygen intermediates. *Chem.—Eur. J.* **2015**, *21*, 17548−17559.
(20) Brinkmeier, A.; Dalle, K. E.; D'Amore, L.; Schulz, R. A.; Dechert, S.; Demeshko, S.; Swart, M.; Meyer, F. Modulation of a μ-1,2-peroxo dicopper(II) intermediate by strong interaction with alkali metal ions. *J. Am. Chem. Soc.* **2021**, *143*, 17751−17760.
(21) Ding, C.; Zhou, X.; Shi, J.; Yan, P.; Wang, Z.; Liu, G.; Li, C. Abnormal effects of cations (Li^+, Na^+, and K^+) on photoelectrochemical and electrocatalytic water splitting. *J. Phys. Chem. B* **2015**, *119*, 3560−3566.
(22) Waegele, M. M.; Gunathunge, C. M.; Li, J.; Li, X. How cations affect the electric double layer and the rates and selectivity of electrocatalytic processes. *J. Chem. Phys.* **2019**, *151*, 160902.
(23) Marcus, Y. Effect of ions on the structure of water: structure making and breaking. *Chem. Rev.* **2009**, *109*, 1346−1370.
(24) Toffoletti, A.; Wang, Z.; Zhao, J.; Tommasini, M.; Barbon, A. Precise determination of the orientation of the transition dipole moment in a Bodipy derivative by analysis of the magneto-photoselection effect. *Phys. Chem. Chem. Phys.* **2018**, *20*, 20497−20503.
(25) Strmcnik, D.; Kodama, K.; van der Vliet, D.; Greeley, J.; Stamenkovic, V. R.; Markovic, N. M. The role of non-covalent interactions in electrocatalytic fuel-cell reactions on platinum. *Nat. Chem.* **2009**, *1*, 466−472.
(26) Monteiro, M. C. O.; Dattila, F.; Hagedoorn, B.; García-Muelas, R.; López, N.; Koper, M. T. M. Absence of CO_2 electroreduction on copper, gold and silver electrodes without metal cations in solution. *Nat. Catal.* **2021**, *4*, 654−662.
(27) Pérez-Gallent, E.; Marcandalli, G.; Figueiredo, M. C.; Calle-Vallejo, F.; Koper, M. T. M. Structure- and potential-dependent cation effects on CO reduction at copper single-crystal electrodes. *J. Am. Chem. Soc.* **2017**, *139*, 16412−16419.
(28) Resasco, J.; Chen, L. D.; Clark, E.; Tsai, C.; Hahn, C.; Jaramillo, T. F.; Chan, K.; Bell, A. T. Promoter effects of alkali metal cations on the electrochemical reduction of carbon dioxide. *J. Am. Chem. Soc.* **2017**, *139*, 11277−11287.
(29) Singh, M. R.; Kwon, Y.; Lum, Y.; Ager, J. W.; Bell, A. T. Hydrolysis of electrolyte cations enhances the electrochemical reduction of CO_2 over Ag and Cu. *J. Am. Chem. Soc.* **2016**, *138*, 13006−13012.
(30) Zhu, L.; Du, J.; Zuo, S.; Chen, Z. Cs(I) cation enhanced Cu(II) catalysis of water oxidation. *Inorg. Chem.* **2016**, *55*, 7135−7140.
(31) Garcia, A. C.; Touzalin, T.; Nieuwland, C.; Perini, N.; Koper, M. T. M. Enhancement of oxygen evolution activity of nickel oxyhydroxide by electrolyte alkali cations. *Angew. Chem., Int. Ed.* **2019**, *58*, 12999−13003.
(32) Michael, J. D.; Demeter, E. L.; Illes, S. M.; Fan, Q.; Boes, J. R.; Kitchin, J. R. Alkaline electrolyte and Fe impurity effects on the performance and active-phase structure of NiOOH thin films for OER catalysis applications. *J. Phys. Chem. C* **2015**, *119*, 11475−11481.
(33) Görlin, M.; Halldin Stenlid, J.; Koroidov, S.; Wang, H.-Y.; Börner, M.; Shipilin, M.; Kalinko, A.; Murzin, V.; Safonova, O. V.; Nachtegaal, M.; Uheida, A.; Dutta, J.; Bauer, M.; Nilsson, A.; Diaz-Morales, O. Key activity descriptors of nickel-iron oxygen evolution electrocatalysts in the presence of alkali metal cations. *Nat. Commun.* **2020**, *11*, 6181.
(34) Ding, R.; Yasini, P.; Peng, H.; Perdew, J. P.; Borguet, E.; Zdilla, M. J. Reimagining the e_g^1 electronic state in oxygen evolution catalysis: oxidation-state-modulated superlattices as a new type of heterostructure for maximizing catalysis. *Adv. Energy Mater.* **2021**, *11*, 2101636.
(35) Gao, Q.; Ranjan, C.; Pavlovic, Z.; Blume, R.; Schlögl, R. Enhancement of Stability and Activity of MnO_x/Au Electrocatalysts for Oxygen Evolution through Adequate Electrolyte Composition. *ACS Catal.* **2015**, *5*, 7265−7275.
(36) Kang, Q.; Vernisse, L.; Remsing, R. C.; Thenuwara, A. C.; Shumlas, S. L.; McKendry, I. G.; Klein, M. L.; Borguet, E.; Zdilla, M. J.; Strongin, D. R. Effect of interlayer spacing on the activity of layered manganese oxide bilayer catalysts for the oxygen evolution reaction. *J. Am. Chem. Soc.* **2017**, *139*, 1863−1870.
(37) Rao, R. R.; Huang, B.; Katayama, Y.; Hwang, J.; Kawaguchi, T.; Lunger, J. R.; Peng, J.; Zhang, Y.; Morinaga, A.; Zhou, H.; You, H.; Shao-Horn, Y. pH- and cation-dependent water oxidation on rutile RuO_2(110). *J. Phys. Chem. C* **2021**, *125*, 8195−8207.
(38) Zaffran, J.; Stevens, M. B.; Trang, C. D. M.; Nagli, M.; Shehadeh, M.; Boettcher, S. W.; Caspary Toroker, M. Influence of electrolyte cations on Ni(Fe)OOH catalyzed oxygen evolution reaction. *Chem. Mater.* **2017**, *29*, 4761−4767.
(39) Kosasang, S.; Ma, N.; Wuamprakhon, P.; Phattharasupakun, N.; Maihom, T.; Limtrakul, J.; Sawangphruk, M. Insight into the effect of intercalated alkaline cations of layered manganese oxides on the oxygen reduction reaction and oxygen evolution reaction. *Chem. Commun.* **2018**, *54*, 8575−8578.

https://doi.org/10.1021/jacsau.3c00100
JACS Au 2023, 3, 1851−1863

(40) Kim, T. W.; Choi, K. S. Nanoporous $BiVO_4$ photoanodes with dual-Layer oxygen evolution catalysts for solar water splitting. *Science* **2014**, *343*, 990−994.
(41) Zhang, B.; Yu, S.; Dai, Y.; Huang, X.; Chou, L.; Lu, G.; Dong, G.; Bi, Y. Nitrogen-incorporation activates NiFeOx catalysts for efficiently boosting oxygen evolution activity and stability of $BiVO_4$ photoanodes. *Nat. Commun.* **2021**, *12*, 6969.
(42) Zhong, X.; He, H.; Du, J.; Ren, Q.; Huang, J.; Tang, Y.; Wang, J.; Yang, L.; Dong, F.; Bian, L.; Zhou, Y. Boosting solar water oxidation activity and stability of $BiVO_4$ photoanode through the Co-catalytic effect of $CuCoO_2$. *Electrochim. Acta* **2019**, *304*, 301−311.
(43) Trześniewski, B. J.; Digdaya, I. A.; Nagaki, T.; Ravishankar, S.; Herraiz-Cardona, I.; Vermaas, D. A.; Longo, A.; Gimenez, S.; Smith, W. A. Near-complete suppression of surface losses and total internal quantum efficiency in $BiVO_4$ photoanodes. *Energy Environ. Sci.* **2017**, *10*, 1517−1529.
(44) Meng, Q.; Zhang, B.; Fan, L.; Liu, H.; Valvo, M.; Edström, K.; Cuartero, M.; Marco, R. d.; Crespo, G. A.; Sun, L. Efficient $BiVO_4$ photoanodes by postsynthetic treatment: remarkable improvements in photoelectrochemical performance from facile borate modification. *Angew. Chem., Int. Ed.* **2019**, *58*, 19027−19033.
(45) Gao, R.; Wang, L. Stable cocatalyst-free $BiVO_4$ photoanodes with passivated surface states for photocorrosion inhibition. *Angew. Chem., Int. Ed.* **2020**, *59*, 23094−23099.
(46) Zhang, Z.; Huang, X.; Zhang, B.; Bi, Y. High-performance and stable $BiVO_4$ photoanodes for solar water splitting via phosphorus−oxygen bonded FeNi catalysts. *Energy Environ. Sci.* **2022**, *15*, 2867−2873.
(47) Yu, J.; Kudo, A. Effects of structural variation on the photocatalytic performance of hydrothermally synthesized $BiVO_4$. *Adv. Energy Mater.* **2006**, *16*, 2163−2169.
(48) Gotic, M.; Music, S.; Ivanda, M.; Šoufek, M.; Popovic, S. Synthesis and characterisation of bismuth(III) vanadate. *J. Mol. Struct.* **2005**, *744*−*747*, 535−540.
(49) Lee, D.; Wang, W.; Zhou, C.; Tong, X.; Liu, M.; Galli, G.; Choi, K.-S. The impact of surface composition on the interfacial energetics and photoelectrochemical properties of $BiVO_4$. *Nat. Energy* **2021**, *6*, 287−294.
(50) Venugopal, A.; Kas, R.; Hau, K.; Smith, W. A. Operando infrared spectroscopy reveals the dynamic nature of semiconductor-electrolyte interface in multinary metal oxide photoelectrodes. *J. Am. Chem. Soc.* **2021**, *143*, 18581−18591.
(51) Toma, F. M.; Cooper, J. K.; Kunzelmann, V.; McDowell, M. T.; Yu, J.; Larson, D. M.; Borys, N. J.; Abelyan, C.; Beeman, J. W.; Yu, K. M.; Yang, J.; Chen, L.; Shaner, M. R.; Spurgeon, J.; Houle, F. A.; Persson, K. A.; Sharp, I. D. Mechanistic insights into chemical and photochemical transformations of bismuth vanadate photoanodes. *Nat. Commun.* **2016**, *7*, 12012.
(52) Jeong, Y. J.; Seo, D. H.; Baek, J. h.; Kang, M. J.; Kim, B. N.; Kim, S. k.; Zheng, X.; Cho, I. S. Crystal reconstruction of Mo:$BiVO_4$: improved charge transport for efficient solar water splitting. *Adv. Funct. Mater.* **2022**, *32*, 2208196.
(53) Li, C.; Chen, M.; Xie, Y.; Jian, J.; Wang, H.; Jia, L. Boosting the solar water oxidation performance of $BiVO_4$ photoanode via non-stoichiometric ratio drived surface reconstruction. *J. Power Sources* **2022**, *528*, 231242.
(54) Jin, S.; Ma, X.; Pan, J.; Zhu, C.; Saji, S. E.; Hu, J.; Xu, X.; Sun, L.; Yin, Z. Oxygen vacancies activating surface reactivity to favor charge separation and transfer in nanoporous $BiVO_4$ photoanodes. *Appl. Catal., B* **2021**, *281*, 119477.
(55) Regmi, C.; Kshetri, Y. K.; Dhakal, D.; Sohng, J. K.; Rosei, F.; Lee, S. W. Insight into phosphate doped $BiVO_4$ heterostructure for multifunctional photocatalytic performances: A combined experimental and DFT study. *Appl. Surf. Sci.* **2019**, *466*, 787−800.
(56) Wang, L.; Liu, J.; Song, W.; Wang, H.; Li, Y.; Liu, J.; Zhao, Z.; Tan, J.; Duan, Z.; Deng, J. Experimental and DFT insights of $BiVO_4$ as an effective photocatalytic catalyst for N_2O decomposition. *Chem. Eng. J.* **2019**, *366*, 504−513.
(57) Tran-Phu, T.; Fusco, Z.; Di Bernardo, I.; Lipton-Duffin, J.; Toe, C. Y.; Daiyan, R.; Gengenbach, T.; Lin, C.-H.; Bo, R.; Nguyen, H. T.; Barca, G. M. J.; Wu, T.; Chen, H.; Amal, R.; Tricoli, A. Understanding the role of vanadium vacancies in $BiVO_4$ for efficient photoelectrochemical water oxidation. *Chem. Mater.* **2021**, *33*, 3553−3565.
(58) Wang, S.; Wang, X.; Liu, B.; Guo, Z.; Ostrikov, K. K.; Wang, L.; Huang, W. Vacancy defect engineering of $BiVO_4$ photoanodes for photoelectrochemical water splitting. *Nanoscale* **2021**, *13*, 17989−18009.
(59) Pan, Q.; Yang, K.; Wang, G.; Li, D.; Sun, J.; Yang, B.; Zou, Z.; Hu, W.; Wen, K.; Yang, H. $BiVO_4$ nanocrystals with controllable oxygen vacancies induced by Zn-doping coupled with graphene quantum dots for enhanced photoelectrochemical water splitting. *Chem. Eng. J.* **2019**, *372*, 399−407.
(60) Zhang, B.; Sun, L. Why nature chose the Mn_4CaO_5 cluster as water-splitting catalyst in photosystem II: a new hypothesis for the mechanism of O-O bond formation. *Dalton Trans.* **2018**, *47*, 14381−14387.
(61) Zhang, B.; Sun, L. Across the board: licheng sun on the mechanism of O-O bond formation in photosystem II. *ChemSusChem* **2019**, *12*, 3401−3404.
(62) Feng, S.; Wang, T.; Liu, B.; Hu, C.; Li, L.; Zhao, Z.; Gong, J. Enriched surface oxygen vacancies of photoanodes by photoetching with enhanced charge separation. *Angew. Chem., Int. Ed.* **2020**, *59*, 2044−2048.
(63) Lee, D.; Choi, K. Enhancing long-term photostability of $BiVO_4$ photoanodes for solar water splitting by tuning electrolyte composition. *Nat. Energy* **2017**, *3*, 53−60.
(64) Kresse, G.; Furthmüller, J. Efficient iterative schemes for ab initio total-energy calculations using a plane-wave basis set. *Phys. Rev. B* **1996**, *54*, 11169−11186.
(65) Kresse, G.; Joubert, D. From ultrasoft pseudopotentials to the projector augmented-wave method. *Phys. Rev. B* **1999**, *59*, 1758−1775.
(66) Blöchl, P. E. Projector augmented-wave method. *Phys. Rev. B* **1994**, *50*, 17953−17979.
(67) Perdew, J. P.; Burke, K.; Ernzerhof, M. Generalized gradient approximation made simple. *Phys. Rev. Lett.* **1996**, *77*, 3865−3868.
(68) Kim, T. W.; Ping, Y.; Galli, G. A.; Choi, K.-S. Simultaneous enhancements in photon absorption and charge transport of bismuth vanadate photoanodes for solar water splitting. *Nat. Commun.* **2015**, *6*, 8769.
(69) Prakash, J.; Prasad, U.; Shi, X.; Peng, X.; Azeredo, B.; Kannan, A. M. Photoelectrochemical water splitting using lithium doped bismuth vanadate photoanode with near-complete bulk charge separation. *J. Power Sources* **2020**, *448*, 227418.
(70) Grimme, S.; Antony, J.; Ehrlich, S.; Krieg, H. A consistent and accurate ab initio parametrization of density functional dispersion correction (DFT-D) for the 94 elements H-Pu. *J. Chem. Phys.* **2010**, *132*, 154104.
(71) Grimme, S.; Ehrlich, S.; Goerigk, L. Effect of the damping function in dispersion corrected density functional theory. *J. Comput. Chem.* **2011**, *32*, 1456−1465.
(72) Park, Y.; McDonald, K. J.; Choi, K.-S. Progress in bismuth vanadate photoanodes for use in solar water oxidation. *Chem. Soc. Rev.* **2013**, *42*, 2321−2337.
(73) Gu, X.; Luo, Y.; Li, Q.; Wang, R.; Fu, S.; Lv, X.; He, Q.; Zhang, Y.; Yan, Q.; Xu, X.; Ji, F.; Qiu, Y. First-principle insight into the effects of oxygen vacancies on the electronic, photocatalytic, and optical properties of monoclinic $BiVO_4$(001). *Front. Chem.* **2020**, *8*, 601983.
(74) Kalanur, S. S.; Seo, H. An experimental and density functional theory studies of Nb-doped $BiVO_4$ photoanodes for enhanced solar water splitting. *J. Catal.* **2022**, *410*, 144−155.

https://doi.org/10.1021/jacsau.3c00100
JACS Au 2023, 3, 1851−1863